Design and Optimization of High-Efficiency Coreless PCB Stator Axial Flux PM Machines with Minimal Eddy and Circulating Current Losses

Yaser Chulaee, *Student Member, IEEE*, Greg Heins, *Member, IEEE*, Ben Robinson,
Ali Mohammadi, *Student Member, IEEE*, Mark Thiele, *Member, IEEE*,
Dean Patterson, *Life Fellow, IEEE*, Dan M. Ionel, *Fellow, IEEE*

***Abstract*—This paper proposes a systematic multi-step design procedure for highly efficient printed circuit board (PCB) stator coreless axial flux permanent magnet (AFPM) machines with minimal eddy and circulating current losses. The process begins with initial sizing, providing specific coefficients based on experience with multiple design projects. It continues with the optimization of the machine envelope design using an evolutionary algorithm and computationally efficient 3D finite element analysis (FEA) models. The subsequent step focuses on the detailed design of a PCB stator, aiming to minimize eddy and circulating current losses. Several open circuit loss mitigation techniques are proposed based on analytical equations and 3D FEA, while considering PCB manufacturing limitations and standards. The effectiveness of this design procedure is showcased through the design of an integral horsepower PCB stator coreless AFPM machine for HVAC applications, which was prototyped and tested. The experimental results indicated significantly reduced eddy current losses and virtually zero circulating currents, achieving 96% efficiency at a speed of 2,100rpm and an output torque of 19Nm. This outcome validates the efficacy of the proposed approach.**

***Index Terms*—Axial-flux, coreless machines, FEA, optimization, differential evolution, permanent-magnet machines, PCB stator, winding losses, eddy current, circulating current.**

I. Introduction

Permanent magnet synchronous machines (PMSMs), particularly those of axial flux type are being researched and developed for various applications, such as HVAC systems, aviation propulsion, and electric vehicles [1], [2]. The coreless (air-cored) stator axial flux permanent magnet (AFPM) machine topology offers notable advantages over conventional designs by eliminating magnetic cores and their associated losses, including potentially higher efficiency, zero cogging torque, and reduced audible noise and vibration [3], [4].

Lack of a magnetic core in coreless stator machines can also lead to potentially lower weight and volume, depending on the application and system integration. Eliminating the magnetic core allows for more effective cooling systems, wherein the coolant can be in direct contact with the stator windings within liquid-cooled motors, enabling the opportunity to increase current density multiple times that of a conventional cored machine [5], [6]. This can potentially improve power density and specific torque (Nm/kg).

Currently, designers are confronted with the challenge of mitigating stator winding losses, which serves as the primary source of loss in coreless machines. In this type of machine, where there is no magnetic core in the stator, the copper conductors are directly exposed to fluctuations in the airgap's magnetic flux density. This exposure can lead to considerable losses caused by eddy currents [7], [8]. Furthermore, machines with a wide magnetic airgap suffer from an uneven distribution of magnetic flux density and notable flux fringing. Consequently, parallel conductors experience varying induced voltages, resulting in circulating current losses [9], [10].

Lack of a magnetic core presents an opportunity to incorporate printed circuit board (PCB) stators in coreless AFPM machines, which have gained popularity due to their potentially reliable and highly repeatable fabrication process, high modularity, and lightweight nature [11]. The significant flexibility in PCB coil shape designs and their interconnections, with minimal impact on manufacturing setup, presents an excellent opportunity to enhance the efficiency of coreless machines through optimized stator coil designs. As a result, there has been a surge of studies focusing on the design and optimization of PCB coils with the primary objective of minimizing losses and enhancing torque density.

Five different PCB winding topologies were studied and compared in terms of induced voltage, torque, and losses through analytical calculations and finite element analysis in [12], where a novel unequal-width parallel winding was proposed and compared with parallel winding. The trace width of this novel unequal-width parallel winding increases as the radius increases, decreasing the resistance of the copper trace and improving the utilization of the PCB surface area and cooling performance. Another AFPM machine with unequal-width PCB windings with the aim of improving the output power for a small scale wind generator was presented in [13].

A modeling and design procedure for a high-speed 1kW coreless PCB stator multi-phase AFPM machine with non-overlapped windings was proposed in [14], where closed-form equations for torque, eddy current losses, and circulating current losses were utilized. A single-sided axial flux machine with a Halbach array rotor and PCB stator for high-speed applications was introduced in [15], where the machine features distributed non-overlapping coils and the possibility of circulating currents and proximity effects.

A framework for the design and analysis of a commercially

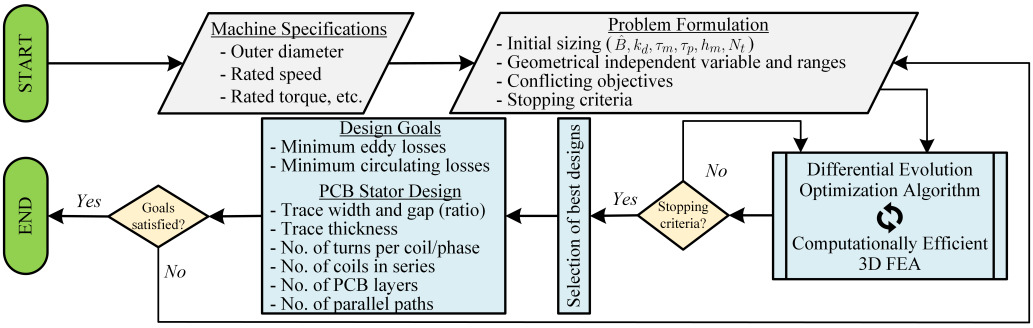

Fig. 1. The flowchart of the introduced multi-step design procedure for PCB stator coreless AFPM machines.

available AFPM machine with a coreless PCB stator and fully integrated variable frequency was presented in [16]. Another example of an integrated compact motor-drive system with a PCB stator was presented in [17], where a genetic algorithm for machine optimization and investigation of open circuit losses was used.

A multi-objective design optimization study for coreless AFPM machine with PCB stator considering AC winding losses was presented in [18]. A PCB stator coreless AFPM machine with wave winding topology was optimized considering a macro coil model to reduce computational burden in [19]. For a coreless stator AFPM machine designed for electric aircraft propulsion systems two PCB stator coil shapes, wave and spiral (concentric), were presented in [20]. Printed circuit board windings can also be utilized for radial flux machines as introduced in [21].

The minimization of eddy current, circulating current, and Joule losses as the stator loss components represents conflicting objectives and cannot be prioritized exclusively. A detailed discussion of the trade-off between stator power loss components was presented by the same group of authors as this paper in [10]. Therefore, a systematic approach is imperative in designing coreless PCB stator AFPM machines that comprehensively considers all stator loss components and the trade-offs between them, while also taking into account PCB stator fabrication limitations and adhering to industry standards. This approach is vital for achieving high efficiency and unlocking the full potential of PCB stator coreless AFPM machines.

This paper is a follow-up expansion of [22] and proposes a systematic multi-step design procedure for PCB stator coreless AFPM machines, considering all stator windings loss components and manufacturing limitations and standards. An exemplary highly efficient integral horsepower PCB stator coreless AFPM machine was specifically designed using this approach, showcasing the effectiveness of the process. All FEA results were obtained from 3D models created in Ansys Electronics Desktop, utilizing the transient solution type [1], [23]. Furthermore, a prototype of the machine was fabricated, and its performance was evaluated through various experimental tests.

II. Design Procedure

The proposed multi-step design procedure is described in this section. In the following sections, an integral horsepower PCB stator coreless AFPM machine is designed and experimentally tested, showcasing the effectiveness of this approach summarized in Fig. 1.

The design procedure begins with the provided specifications of the machine for the designated applications and then continues with problem formulation. In this study, a double-rotor single-stator AFPM machine for a fan application serves as an example. Axial flux machines have various configurations, and among them, the dual rotor single-stator design is prevalent due to its robustness and high torque density [16]. The exploded view of this configuration is demonstrated in Fig. 2a. This machine is expected to deliver a rated torque of 19Nm at 2,100rpm (≈4.2kW) with an outer diameter of 310mm, constrained by the dimensional requirements for mechanical integration.

A. Initial Sizing

The AFPM machines sizing equation reveals that the electromagnetic torque varies cubically with its outer diameter, D_o, as detailed in [2], [4]. Another crucial design factor is the ratio of inner to outer diameter, denoted as $k_d = D_i/D_o$. This ratio should fall within the range $[0.65, 0.75]$ for designs targeting high power density [2].

For a non-salient double rotor AFPM machine as shown in Fig. 2a, the fundamental component of the airgap flux density in the axial direction can be expressed as [24]:

$$B_{z,1}(\theta, z) = \hat{B} \cosh\left(\frac{\pi}{\tau_p} z\right) \cos(\theta), \tag{1}$$

with the peak value of:

$$\hat{B} = \frac{4B_r}{\pi} \frac{\sinh[\pi(k_\sigma k_b h_m/\tau_p)]}{\sinh[\pi(k_c g/2\tau_p)]} \sin\left(\frac{\pi}{2} k_m\right), \tag{2}$$

where B_r is the remanence of the PMs, τ_p the pole pitch, h_m the magnet thickness, g the airgap length, i.e. magnet to magnet distance as shown in Fig. 4, and $k_m = \tau_m/\tau_p$ the magnet arc length to pole-pitch ratio. Considering this equation, for a target airgap flux density and a specified magnet type the dimensions of the magnets can be decided [25].

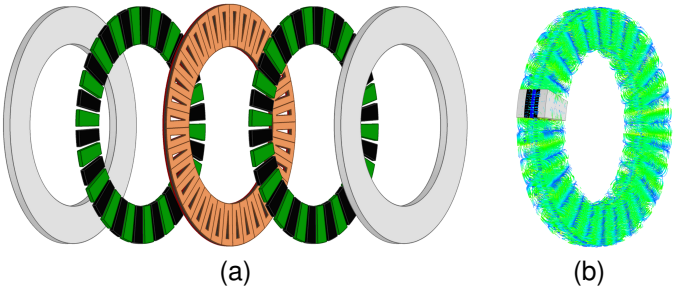

Fig. 2. The exploded view of the double-rotor single PCB stator coreless AFPM machine configuration (a). Full model flux density lines of the example coreless AFPM machine (b). The design optimization and other studies were done based on 3D FEA models, but employing an ultra-fast model that takes advantages of the machine symmetry and minimum number of FEA solutions.

Carter's and PM leakage coefficients are represented by k_σ and k_c, respectively. Both can be approximated with a unity value for surface PM (SPM) coreless machines. The coefficient k_b is equal to the number of PMs that provide the polar flux with a unity value for SPM. The calculated waveform based on (1), is shown in Fig. 4.

For a given fundamental rated phase voltage, $\hat{V}_{ph,1}$, and considering the calculated magnetic flux density in the airgap, the number of turns per phase can be estimated as:

$$N_t = \frac{k_u\ \hat{V}_{ph,1}}{2\pi\ f_1\ \Psi_{PM}} = \frac{4p\ k_u\ \hat{V}_{ph,1}}{\pi^2 f_1\ k_{w1}\ k_{avg}\ k_m\ \hat{B}\ D_o^2\ (1-k_d^2)}, \tag{3}$$

where k_u represents the ratio of back-EMF (i.e., open circuit voltage) to induced voltage (i.e., generated voltage at the rated current), which is typically close to one for coreless machines, f_1 the rated fundamental frequency, p the number of pole-pairs, k_{w1} the fundamental winding factor, and k_{avg} the ratio of the fundamental to the average value of the airgap flux density, which depends on certain geometrical dimensions such as magnet arc length. Typically, for SPMSMs, k_{avg} falls between $1.1/k_m$ and $\pi/2$ [25]. In this equation, Ψ_{PM} denotes the open-circuit PM flux linkage.

The electromagnetic torque can be estimated by:

$$T_{em} = \frac{m}{2}\ p\ \Psi_{PM}\ J_{rms}\ SFF\ c_w\ \ell_c/N_t, \tag{4}$$

where m is the number of phases, J_{rms} the current density in copper conductors, c_w the coil side width, ℓ_c the coil axial thickness, and SFF the slof-fill-factor.

The 3D flux pathways, multiple geometry-dependent coefficients, and complicated PCB coil geometry affect the accuracy of the analytical equations, leading to unsatisfactory results. The calculated fundamental component of the airgap flux density, based on (1), was compared with FEA results, showing an approximately 15% error in the average value, as depicted in Fig. 4. This average value was then used to calculate the flux linkage Ψ_{PM}. The inaccuracy is mainly due to the large variations in flux lines, both in the circumferential and axial directions, as shown in the cross-sectional view of Fig. 4, which are not captured in the analytical equations.

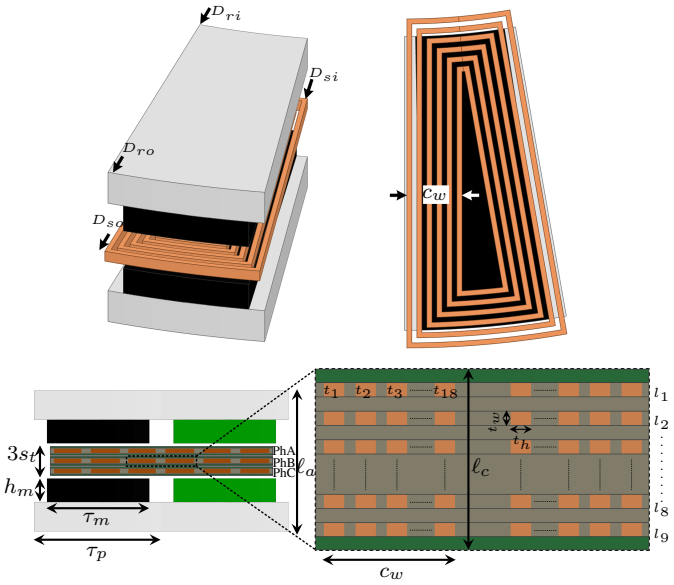

Fig. 3. The 3D FEA parametric model of one pole with the simplified PCB coil employed in the design optimization study. The detailed view of the real PCB coil cross section is also shown.

Hence, there is a need for 3D FEA models to ensure the accuracy of performance estimation. These models demand extensive computational power and long running times. The computation time becomes even more prolonged in the case of PCB stator machines with complex models, including narrow copper traces that necessitate a large number of mesh elements.

Solving hundreds of such 3D FEA models within an optimization study on regular workstations poses a significant challenge. Therefore, there is a need for computationally efficient 3D FEA models for AFPM machines. To address this issue, a FEA-based mathematical method is introduced, using the minimum number of FEA solutions possible and thereby significantly reducing running time.

B. Computationally Efficient 3D FEA (CE-FEA) Model

The single-phase output torque waveform of an example coreless AFPM machine resulting from a transient FEA with 36 time steps is shown in Fig. 5. The single-phase torque here refers to the output torque generated solely by one phase (one PCB stator), while the total output torque is derived by summing such waveforms that are shifted by 120 degrees with respect to each other. The general expression of single-phase torque waveform in the form of a Fourier series can be written as follows:

$$T_{em}(\theta) = T_{em,0} + \sum_{k=1}^{M} T_{em,k}\ \cos(k\theta + \phi_k)\ , \tag{5}$$

where

$$\begin{aligned} T_{em,0} &= \frac{1}{\pi}\int_0^\pi T_{em}(\theta)\ \mathrm{d}\theta\ , \\ T_{em,k} &= \frac{2}{\pi}\int_0^\pi T_{em}(\theta)\ \cos k\theta\ \mathrm{d}\theta\ , \end{aligned} \tag{6}$$

θ is rotor position in electrical degrees, ϕ the initial degree for each phase, and M is the highest order of harmonics present in the signal.

The harmonic content of the single-phase torque waveform was derived from a conventional Fourier series analysis and is tabulated in Table I. Here, one electrical cycle, i.e., 0 to 360 electrical degrees, was considered as its period. The results indicate that the DC component and the second harmonic contribute the majority of the harmonic content, while the fourth harmonic order represents only 1.1% of the second harmonic, and the rest of the harmonic orders are virtually zero.

According to the Nyquist theorem, for a complete representation of Fourier components in a periodic waveform, the sampling frequency, f_s, must be at least twice the highest frequency component, f_m. Consequently, to construct a waveform, the number of FEA solutions, s, must be equal to or greater than twice the maximum harmonic order, M: $s \geq 2M$.

To accurately capture the torque waveform under investigation, considering up to the second harmonic yields satisfactory results as it contains the majority of its harmonic content. Hence, with M=2, a minimum of four FEA solutions are necessary. Since the torque waveform repeats every 180 electrical degrees, we intuitively know that only two FEA solutions are required. This method, circumventing unnecessary FEA solutions, significantly cuts down the time required for model analysis while upholding result accuracy.

The calculated torque waveform within one electrical cycle, with only two FEA solutions at 0 and 90 electrical degrees, is shown in Fig. 5. It is worth mentioning that there is no need to have the two FEA solutions exactly at 0 and 90 electrical degrees. Exactly the same analysis approach is applicable to flux linkage and by taking the derivative of it and considering the motor speed, the machine back-EMF was derived, as depicted in Fig. 5.

It is important to highlight that the absence of a magnetic core, and consequently, saturation effects, leads to a reduced harmonic content in coreless machine flux density and torque waveforms. This facilitates predicting the machine's performance with fewer finite element analysis solutions. The systematic approach introduced to achieve the most accurate and computationally efficient results is generally applicable to coreless machines, even in the presence of marginal saturation due to specific designs. The absence of saturation in coreless AFPM machines was investigated in [24] and [26] by studying their performance under various conditions through FEA-based parametric studies.

Taking into account the geometric and magnetic symmetry of the machine, only one pole with a reduced-turn PCB coil that is able to effectively replicate the current trajectories in real PCB coils was modeled, as shown in Fig. 3. This model results in a significant reduction in computational time.

C. Stator Design and Loss Minimization

The next step is dedicated to optimizing the machine envelope, i.e., stator and rotor dimensions, to achieve predetermined objectives, which are considered based on the requirements of any specific application. In the design optimization of electric machines, geometrical variables, the number of pole pairs, and material constants are typically treated as independent variables. The optimization is done by evaluating hundreds of candidate designs that in this case are 3D FEA models of the machine. Within the optimization study, the independent variables are adjusted by a systematic algorithm, seeking the optimum designs that satisfy the objectives. It is also essential to establish a stopping criteria for the optimization algorithm.

The final step focuses on designing the PCB stator layout for the given optimized envelope. All details of the PCB coils such as number of turns, number of layers, trace width, trace thickness, clearance between traces, and interconnections are determined in this step. The designed PCB stator must deliver the desired output power requirement with a minimized power losses in the windings. Within this step, analytical equations for calculating eddy and circulating current losses along with several proposed loss mitigation techniques are described.

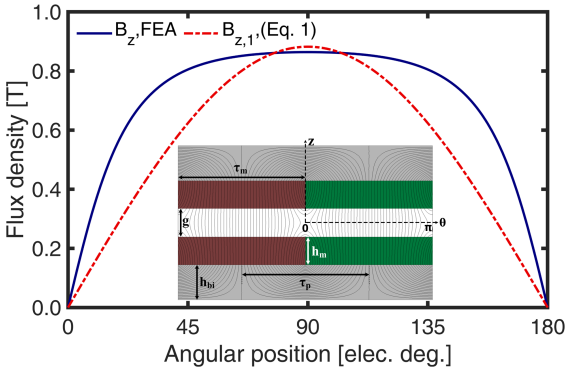

Fig. 4. The airgap flux density, B_z, of the double-rotor coreless AFPM machine derived from FEA within half of an electrical cycle. The amplitude of the fundamental component of B_z based on FEA is 1.01T. The analytically calculated fundamental component, $B_{z,1}$, based on (1), is also shown.

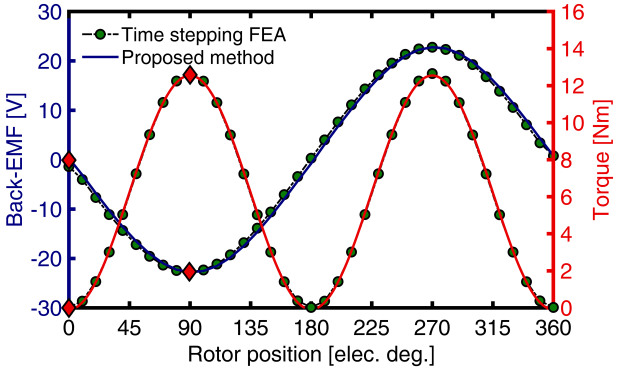

Fig. 5. The single-phase output torque and back-EMF derived from a transient FEA with 36 time steps. The calculated waveforms based on only two FEA solutions at 0 and 90 electrical degrees (marked by ♦), are also shown.

TABLE I
THE SINGLE-PHASE TORQUE WAVEFORM HARMONIC CONTENT. ALL HARMONIC ORDERS HIGHER THAN FOUR ARE ZERO.

Harmonic order	a_0 [Nm]	a_k [Nm]	b_k [Nm]
DC Component	6.23	-	-
First	-	0.00	0.00
Second	-	-6.32	0.00
Third	-	0.00	0.00
Fourth	-	0.07	0.00

III. DESIGN OPTIMIZATION

This step involves optimizing the machine envelope for predetermined objectives through the use of the multi-objective differential evolution (MODE) optimization algorithm and CE-FEA models. For HVAC fan motors that were considered as the target application in this research, manufacturers and customers typically prioritize cost competitiveness and efficiency [27]. Therefore, two objectives were considered: the minimization of magnet mass M_{PM}, which is the main contributor to the machine's total cost, and the minimization of Joule losses P_J, the major source of power losses:

$$\begin{aligned} F_1 &= M_{PM} = \frac{\pi}{4}\ \rho\ k_m\ h_m\ \left(D_{ro}^2 - D_{ri}^2\right), \\ F_2 &= P_J = m\ N_c\ \rho_{cu}\ \ell_m\ \ell_c\ c_w\ SFF\ J_{rms}^2, \end{aligned} \tag{7}$$

where ρ is the mass density of PMs, N_c the total number of coils per phase, ρ_{cu} resistivity of copper, and ℓ_m average length of a coil. The magnet material is Neodymium (NdFeB), with a mass density of 7400 kg/m^3 and a relative permeability of 1.05.

It needs to be mentioned that eddy and circulating current losses within the stator windings will be separately studied and minimized for the designed layout based on the optimized coil envelope. The absence of a magnetic core in stator coreless machines results in a very low armature reaction, meaning negligible magnetic field generation by stator windings and, consequently, virtually zero eddy current losses in the rotor magnets and back iron.

For this optimization study, seven geometric independent variables were considered, as listed in Table II and illustrated in Fig. 3. The outer diameter of the stator was set to 310mm, and its inner diameter was determined by the stator split ratio, k_{sr}. The overhang ratio, represented by k_{oh}, governs the proportion of the magnet radial length to the stator coil radial length. When k_{oh} is equal to one, the rotor magnets completely cover the end coil. To avoid saturation, the thickness of rotor back iron was also fixed at 10mm [24].

The optimization algorithm discovers optimal designs, i.e., the Pareto front, by adjusting the independent variables. The design optimization process was fully automated by integrating Ansys and MATLAB using the scripting feature. The population size of each generation was set to 40, which is six times larger than the number of independent variables. If there is only a minor improvement in three selected points on the Pareto front for several consecutive generations, the optimization process is terminated.

TABLE II
GEOMETRICAL INDEPENDENT OPTIMIZATION VARIABLES AND CORRESPONDING LIMITS FOR THE TARGETED MACHINE SPECIFICATIONS.

Var.	Description	Min	Max
g	Airgap [mm]	0.75	1.50
k_{sr}	Stator split ratio, $\frac{D_{si}}{D_{so}}$	0.65	0.85
k_{oh}	Overhang ratio, $\frac{D_{ro}-D_{ri}}{D_{so}-D_{si}}$	0.57	1.00
c_w	Coil side width [mm]	7.00	9.00
k_m	PM coverage ratio, $\frac{\tau_m}{\tau_p}$	0.80	1.00
h_m	PM thickness [mm]	3.00	7.00
s_t	Stator thickness [mm] (single phase)	1.12	3.00

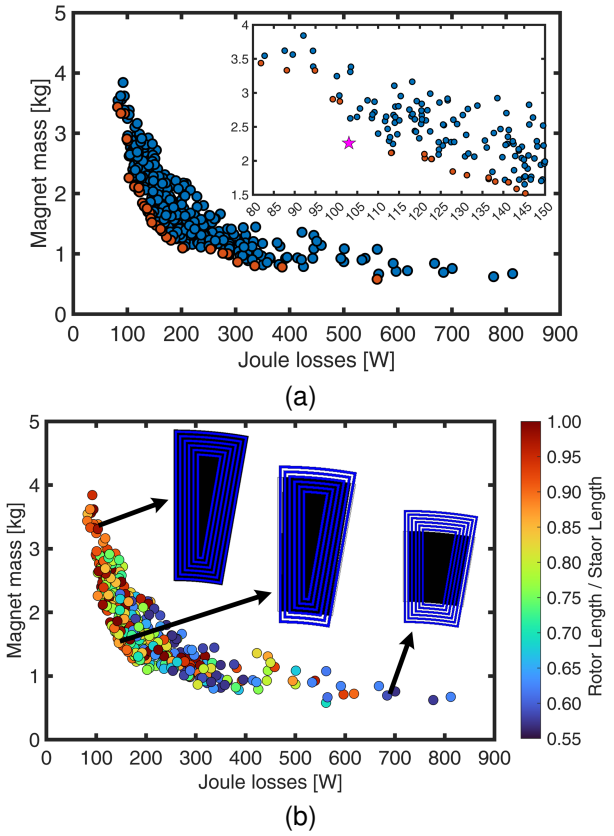

Fig. 6. All the designs evaluated in the optimization study, with the Pareto front shown as orange dots (a). The overhang ratios, i.e., rotor length to stator length ratios, for all the designs within the optimization results are shown as color code (b).

The search space for the optimal design is designated to be extensive, indicating that the optimization variables have wide ranges, with the sole exception of geometrical restrictions. These restrictions are implemented to avoid interference between different geometric components and to account for mechanical limitations, such as the minimum air gap and standard PCB thicknesses.

The design optimization process concluded after 12 generations, during which 480 candidate designs were evaluated. All

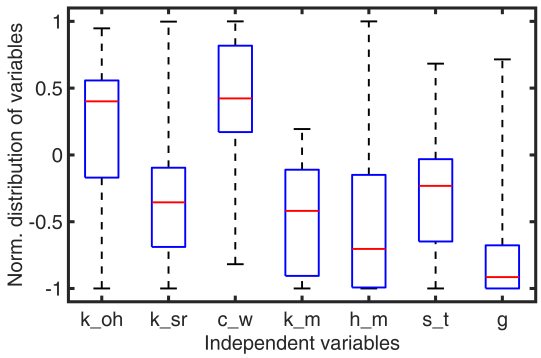

Fig. 7. The normalized distribution of the independent variables for the Pareto front designs.

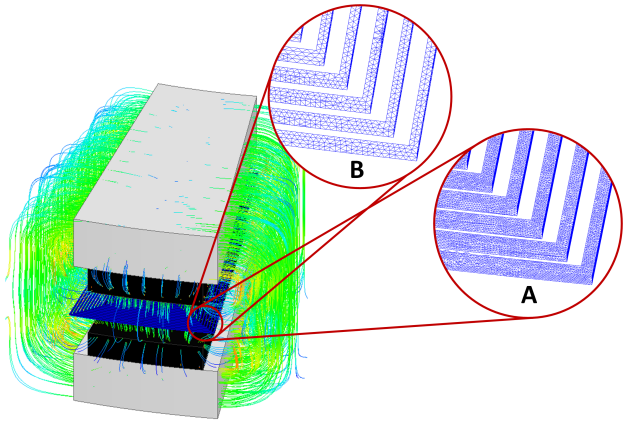

Fig. 8. Flux lines of the 3D FEA model and the tetrahedral mesh elements on the designed PCB coil model for eddy current loss calculation. To ensure the accuracy of the results, a mesh convergence study was carried out.

designs and the Pareto set are illustrated in Fig. 6a. It's worth noting that all designs produce the same predetermined rated output torque with their corresponding current densities.

Solving the proposed simplified 3D FEA model for two solutions takes approximately 6 minutes on the available workstation in the research laboratory equipped with an Intel® Xeon® 3.5-GHz processor, and the entire optimization process was finished in less than 42 hours. Solving the detailed turn-by-turn 3D model of the PCB coil shown in Fig. 8 requires millions of mesh elements and approximately 10 hours to solve for just one solution, rendering its integration into large-scale optimization studies impractical.

The normalized distributions of the optimization independent variables for the Pareto front designs are demonstrated as box plots in Fig. 7. Apart from the airgap, all the variables seem to be positioned comfortably far away from the bands, indicating that appropriate limits have been predetermined. It is also observed that the optimal designs within the Pareto front tend towards having a narrower airgap. Furthermore, the corresponding overhang ratio for each design is shown in Fig. 6b as a color code.

The results indicate that most of the relatively heavyweight designs with low copper losses have higher overhang ratios, meaning that rotor PMs cover the majority of the end coils. The reason for this is that larger magnets in the radial directions cover the corners of the coils at both ends, leading to the production of more torque with lower current and consequently fewer Joule losses, as well as a higher magnet volume.

It should be noted that assuming designs with higher overhang ratios will result in superior efficiencies is inaccurate. Larger magnets in radial directions cover the end coils (i.e., copper conductors in the circumferential direction) that do not contribute to torque production and only increase eddy current losses, which lowers efficiency.

Designs that are positioned close to the knee point on the Pareto front have rotor PMs that partially encase the end coils. These designs exhibit lower eddy current losses while maintaining a favorable balance between magnet mass and Joule losses. Therefore, such designs can feature potentially lower total copper losses as it has been demonstrated for the designed layout in Fig. 12.

It should be noted that, according to (7), the copper losses of the actual coil can be derived by scaling the copper losses of the simplified coil with the ratio of SFFs. It is assumed that both the simplified and the actual coils have an equivalent magnetomotive fore (MMF), producing exactly the same output torque. At this stage, a typical SFF of 0.20 for PCB coils, based on previous research studies by the same group of authors, was considered for scaling [19], [20].

Considering the rated specifications and taking into account manufacturing restrictions and standards, a preliminary calculation was conducted, and out of the designs that met the criteria of weighing less than 2.5kg and having Joule losses under 150W, one was chosen for the subsequent stage of the design process. The selected design is marked by a star as shown in the zoomed-in view in Fig. 6a. It should be noted that the actual PCB coil will be designed in the next step, considering the optimized coil envelope established at this stage.

IV. Detailed Design of PCB Stator Layout

This step focuses on the detailed design of the PCB stator, taking into account the provided stator coil envelope for the selected design. During this process, the simultaneous minimization of all stator loss components, namely eddy current losses, circulating current losses, and Joule losses, is taken into consideration. The optimized coil envelope is shown in Fig. 3.

A. Eddy Current Loss Analysis and Proposed Mitigation Technique

The eddy current losses per phase for PCB traces with rectangular cross sections, as demonstrated in Fig. 3, can be calculated as follows:

$$P_{ed} = \frac{\pi^2 \; N_{cs} \; N_t \; N_p \; f^2 \; t_w \; t_h \; l_m}{6\rho} \left(t_w^2 \; B_z^2 + t_h^2 \; B_\phi^2 \right), \quad (8)$$

where N_{cs} represents the number of coil sides. The terms B_z and B_ϕ refer to the axial and tangential components of the

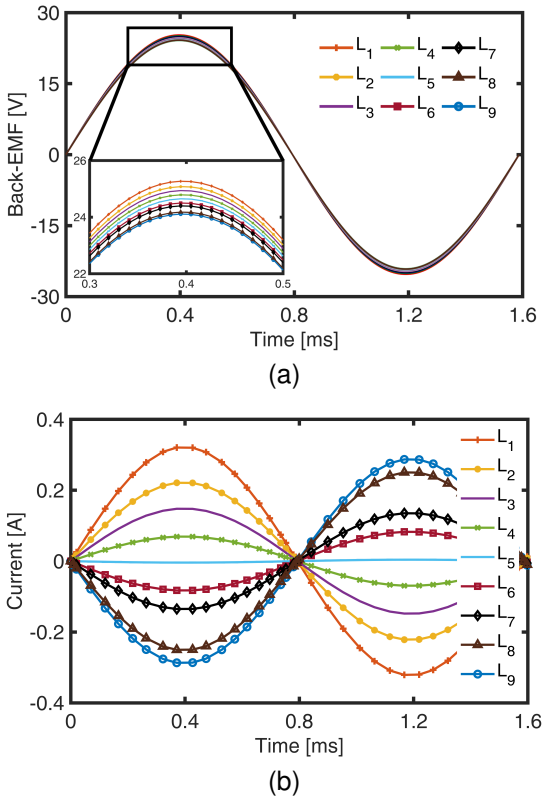

Fig. 9. The induced voltages in nine parallel coils under one pole ($C_{1,L1}$ to $C_{1,L9}$) placed in nine layers (a) and corresponding circulating currents within these coils due to voltage difference between parallel paths in the absence of layer transposition (b). It highlights the necessity of having layer transposition to balance induced voltages and eliminate circulating currents.

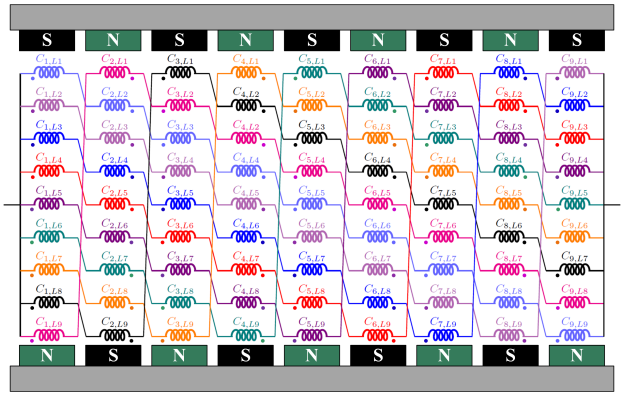

Fig. 10. The diagram of the layer transposition for a 9-layer PCB stator with 9 coils in series. Each parallel path is denoted by a distinct color for better demonstration.

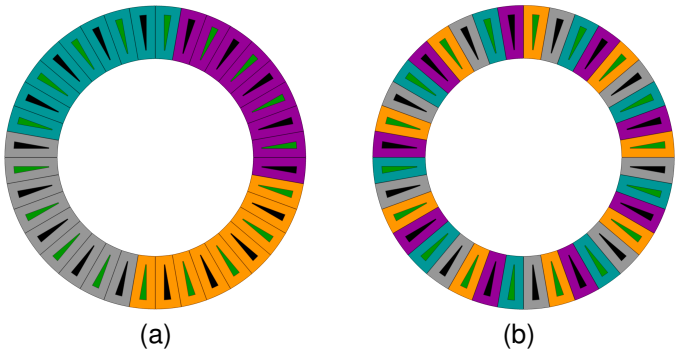

Fig. 11. The coils distributions around the PCB stator within one phase (a) and (b). Coils in each parallel path are shown in the same color. Evenly distributing coils around the stator, as shown in (b), effectively reduces circulating currents between parallel paths in the presence of rotor imbalances and an uneven airgap.

flux density, respectively. Furthermore, t_w denotes the trace width, t_h represents the trace height in the z-direction, and f denotes the frequency of flux variations [28], [29].

This equation implies that the magnitude of eddy current losses is proportional to the cube of the trace width, emphasizing the minimization of trace width to avoid high eddy current losses. The minimum trace width is limited by the PCB manufacturer's capabilities and standards. Moreover, decreasing the trace width has the disadvantage of lowering the SFF and the current-carrying capacity of the phase winding.

The proposed approach is designing PCB coils with narrow but axially thick traces. Since the tangential component of the airgap flux density, B_ϕ, is insignificant, designing PCB coils with relatively thick traces compensates for the reduction in SFF and current-carrying capability caused by narrow traces, with no considerable impact on eddy current losses. The detailed trace by trace model employed for eddy current loss analysis with different trace width and thickness is shown in Fig. 8.

Fabricating thick copper traces with a narrow width is challenging, and one must consider the minimum trace width to trace height ratio, i.e., t_w/t_h, provided by the manufacturers. Hence, the practical and effective approach to enhance current-carrying capability and reduce Joule losses, while concurrently minimizing eddy current losses, is to first increase the thickness of traces as much as possible, and then use multiple identical coils in different layers connected in parallel. However, this may lead to high circulating current losses in the stator, a loss component addressed in the following section.

B. Circulating Current Loss Analysis and Proposed Mitigation Techniques

Due to the non-uniform airgap flux density in coreless AFPM machines caused by a wide magnetic airgap and flux fringing effect, axially distributed parallel coils experience varying magnetic flux, resulting in different induced voltages and, consequently, circulating current losses. For the designed machine an example of circulating currents caused by variations in induced voltages within nine coils axially distributed between two rotor magnets are illustrated in Fig. 9a and 9b. These results were derived from FEA and in this case the distance between the first and last coil is only two millimeters (the PCB thickness). A detailed investigation of circulating current losses was presented in [10] and [30].

The circulating current losses within n parallel paths, each with an equal resistance of R and an induced voltage denoted

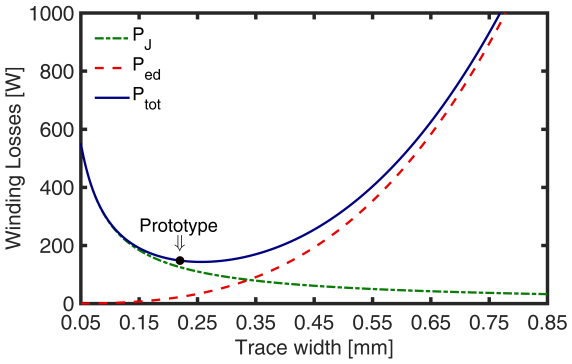

Fig. 12. The variations in eddy current losses and Joule losses versus the copper trace width at the rated condition. The accumulated copper losses of the designed prototype, with a trace width of 0.22mm, are close to the minimum value.

by E_i for the i^{th} path, can be expressed as given in [10]:

$$P_{cr} = \sum_{i=1}^{n} RI_i^2 = \frac{1}{R}\sum_{i=1}^{n}\left[E_i - \frac{\sum_{i=1}^{n} E_i}{n}\right]^2. \quad (9)$$

To mitigate circulating currents, it is necessary to balance the flux linkages within parallel paths. To achieve this balance, a complete layer transposition is proposed as an effective technique to geometrically balance the induce voltages within parallel paths. This ensures that all axially distributed parallel paths are equally affected by the airgap flux density variation, thereby creating similar induced voltages.

Effective implementation of layer transposition requires numerous interconnections between coils in different axial positions, as well as precise coil placement. Hence, PCB stators are highly suitable candidates for such arrangements due to the flexibility in designing coil shapes and interconnections, as well as the automated, precise CAD-based manufacturing process.

A complete layer transposition for nine parallel sets of coils, each including nine coils in series, is demonstrated in Fig. 10. In the presence of layer transposition, although the induced voltages in axially distributed coils, such as $C_{1,L1}$ to $C_{1,L9}$, remain as depicted in Fig. 9a, circulating currents are virtually zero, as all nine parallel paths have the same potential. This is achieved because each parallel path, denoted by a distinct color in Fig. 10, includes nine coils distributed across all nine layers of the PCB, representing different axial positions.

For a complete and effective implementation of layer transposition, coordination among the number of parallel layers, coils in series, and poles is necessary. The optimal combination is when the number of coils in series equals the number of parallel coils (PCB layers), as illustrated in Fig. 10. It should be noted that the number of coils in series per phase is determined by the number of turns per coil and the required rated back-EMF. For a constant back-EMF, a lower number of coils in series leads to coils with a higher number of turns and very narrow traces, and vice versa. Therefore, the number of poles plays a key role in implementing complete transposition. This number needs to be divisible by multiple numbers to facilitate the design process. In this instance, 36 poles were selected because this number allows for divisibility by 2, 3, 4, 9, 12, and 18, thereby offering flexibility in the design process.

It is worth mentioning that coreless machines can be designed with a higher number of poles since frequency-dependent core losses have been eliminated, resulting in smoother operation. It should be noted that if the number of coils in series or the number of pole pairs does not meet other design considerations, one should return to the previous step and make modifications accordingly. It is important to highlight that within a PCB stator with n layers, the implementation of layer transposition does not affect production costs; rather, it only demands careful consideration in the layout design procedure.

Axial flux machines are also susceptible to manufacturing imperfections, such as uneven airgaps and rotor eccentricity. These imperfections may result in circulating current losses between the parallel coils distributed around the stator. For instance, if, in this case, each set of nine series coils within one parallel path is grouped together to reduced interconnections, as shown in Fig. 11a, one group of coils may experience higher flux linkage due to a smaller airgap in the presence of an unbalanced rotor. This imbalance leads to a higher induced voltage in one path and, consequently, circulating current losses [10].

To address this issue, coils in different parallel paths need to be evenly distributed around the stator, as demonstrated in Fig. 11b. This coil configuration effectively enhances the stator's tolerance against rotor manufacturing tolerances.

C. Selection of Final PCB Stator Layout

Considering the proposed methods to mitigate winding losses, the design of the PCB stator begins by choosing a trace width as narrow as 0.22mm, which is close to the minimum limit for a copper thickness of 3oz. It should be noted that 3oz. is the maximum copper mass equivalent to a copper thickness of 0.105mm, in order to keep the t_w/t_h ratio within the range allowed in the standard PCB manufacturing process.

To fulfill the back-EMF requirement at the rated speed, a total of 162 turns per phase is needed. To accommodate the given optimized coil side width without violating the minimum standard clearance between traces (approximately 0.20mm), nine coils in series, each with 18 turns, need to be considered.

Additionally, to meet the required MMF while maintaining the current density in PCB traces within the standard range and improving the SFF, nine sets of such coils need to be connected in parallel. These sets of coils are distributed across a ten-layer PCB, with one layer dedicated to interconnecting them. To enhance further current-carrying capability, four sets of coils, as shown in Fig. 10, were distributed around the stator and connected in parallel, resulting in a 36-pole stator, as depicted in Fig. 11b. It should be noted that the previously introduced layer transposition must be considered to mitigate circulating current losses.

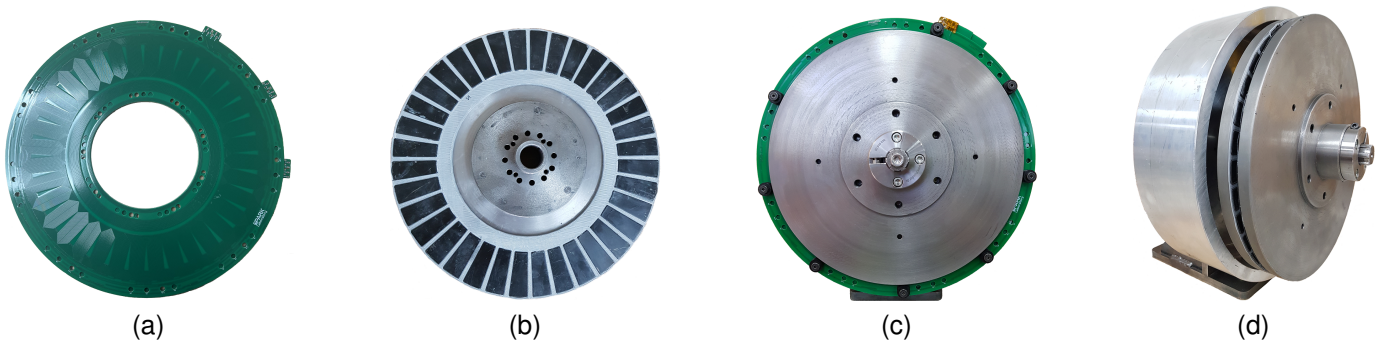

Fig. 13. The prototype 3-phase double-rotor coreless AFPM machine with a rated torque of 19Nm at 2,100rpm (a) and (b). The fabricated PCB stators are stacked together and mechanically shifted by 6.66 degrees, equivalent to 120 elec. deg., to form a 3-phase stator (c). The 36-pole permanent magnet rotor with NdFeB PMs (d).

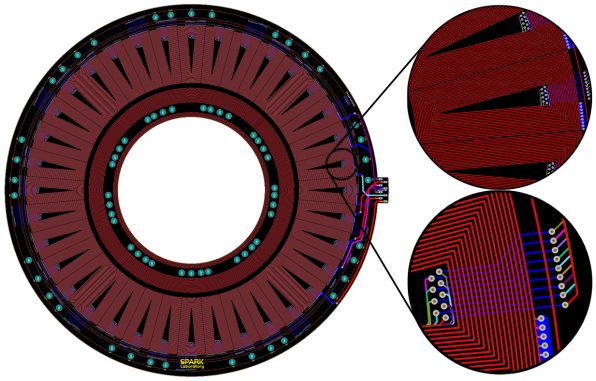

Fig. 14. The designed 36-pole PCB stator with 9 active layers and one layer for other connections. Note the very narrow traces with a width of 0.22mm, which greatly reduce eddy current losses.

The CAD model of the designed PCB stator for fabrication is illustrated in Fig. 14. The connections between coils in different layers, necessary for the implementation of layer transposition, were established through via holes, as depicted in the zoomed-in view of this figure.

A parametric study illustrating variations in eddy current and Joule losses versus trace width at the rated power for the designed PCB stator, derived from a 3D FEA, is shown in Fig. 12. This study reveals that the stator designed following the proposed approach has accumulated losses near the minimum value. The detailed experimental investigation of power losses is presented in the next section.

V. Prototype Machine and Experimental Results

The designed machine was prototyped, and the accuracy of the developed 3D FEA models, as well as the effectiveness of the proposed loss mitigation techniques, were experimentally validated. The assembled prototype machine along with a view of the rotor magnets and the fabricated PCB stator are shown in Fig. 13.

The performance and dimensional specifications of the prototype are provided in Table III. It is worth mentioning that the slot fill factor (SFF) of the fabricated PCB coils is 0.20, and the substrate material is FR4. It should be noted that PCB coils typically exhibit a low SFF due to manufacturing standards and limitations, such as predetermined minimum t_w/t_h ratio and minimum insulation layer thickness. Employing new substrate materials or heavy copper PCBs within advanced premium manufacturing processes can potentially improve SFF.

To measure back-EMFs, the prototype machine was coupled to a three-phase 3.8kW PMSM servomotor (AKM2G series) as the prime mover, with its speed controlled by a 4.0kVA drive system (AKD2G series), both manufactured by Kollmorgen, as shown in Fig. 15a. The prototype machine rotated up to its rated speed of 2100rpm and a YOKOGAWA DL850 oscilloscope was used to record waveforms with high resolution. The measured three-phase rated back-EMFs are compared with FEA results in Fig. 16, demonstrating a high level of agreement. The mechanical airgap (magnet to stator) was set to 1.3mm for the preliminary experiments.

The torque constant was verified by measuring static torque at different input currents. For static torque measurement, the rotor was locked in position at 90 electrical degrees with respect to the phase A axis, where it generates maximum torque per ampere, using a 14kW electronically controlled hysteresis brake (HD series) manufactured by Magtrol. Subsequently, a gradually increasing DC voltage was applied to the motor phases. The test setup, along with the standard circuit diagram for static torque measurement, is depicted in Fig. 15b [31].

A non-contact torque sensor was placed between the prototype motor and the brake to measure the output torque. The applied current corresponding to the rated torque was used to calculate Joule losses, taking into account the measured phase resistance. The measured and calculated torque constant and Joule losses are reported in Table IV.

To measure the open circuit winding losses, i.e., eddy and circulating current losses, several spindown tests were conducted. As part of the spin-down test, the introduced prime mover initially rotated the tested prototype, with the terminals of the phase windings left unconnected (i.e., in open circuit). Once the machine reached its rated speed, the prime mover was disengaged using a fast actuator, and the speed profile from the rated value to zero was recorded using a Hall effect

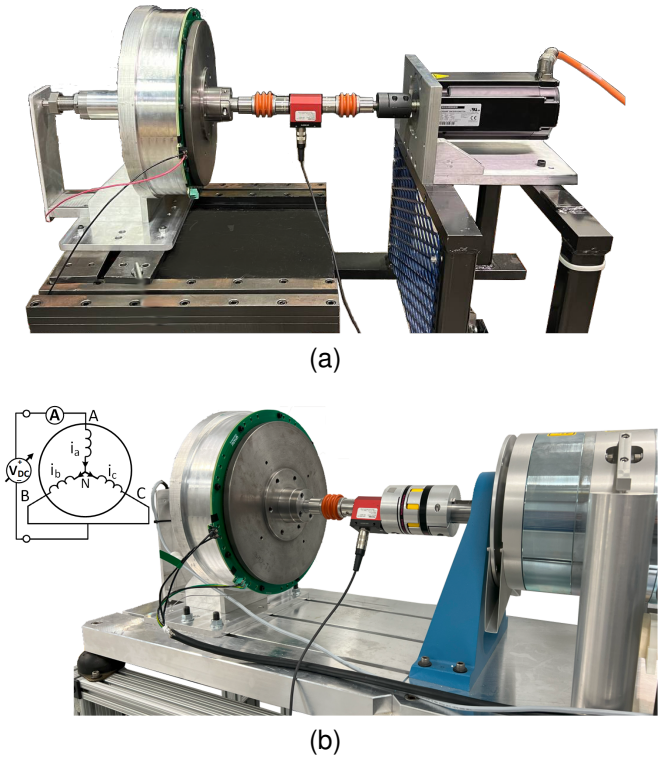

Fig. 15. The test setup includes (a) a PM synchronous speed-controlled servomotor used as a prime mover for back-EMF measurement and spindown tests, and (b) a prototype machine coupled with an electronically controlled hysteresis brake for static torque measurements. The standard circuit diagram for static torque measurement is also shown [31].

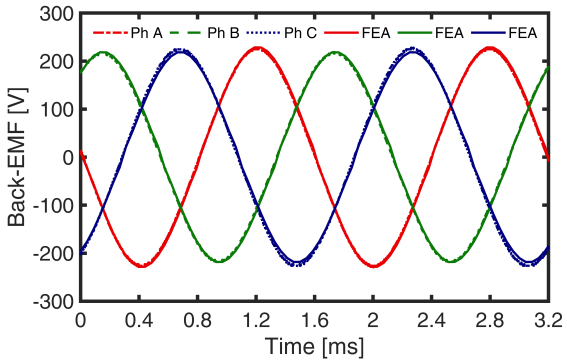

Fig. 16. The measured three-phase back-EMFs of the prototype machine, when compared with the results of the finite element analysis, show a very good agreement between the two sets of results.

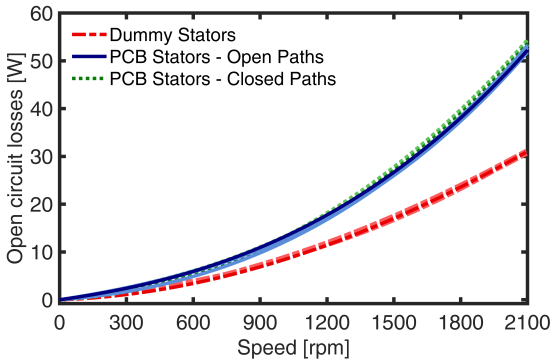

Fig. 17. Spindown tests results for measuring the mechanical and the stator open circuit losses.

speed sensor. For this prototype, it took approximately 50 seconds to decelerate from the rated speed to zero due to the large inertia of the rotor. It is worth mentioning that axial flux machines feature relatively high inertia compared to radial flux counterparts, primarily because of the large diameter of the rotor and its narrow axial length.

Based on the fundamental torque equation of motor-load systems and using the measured speed profile and calculated rotor inertia the total open circuit power losses, including eddy and circulating current losses, can be derived [32], [33]. To separate mechanical losses (i.e. friction and windage) the described test needs to be repeated with dummy plastic stators.

To differentiate between eddy and circulating current losses, the terminals of the parallel paths were brought out of the PCB stator during the design process. The tests were then repeated with and without connecting the parallel paths. Subtracting the measured losses in these two tests provided the circulating current losses. The calculated power loss profiles result from the spindown tests are depicted in Fig. 17 and detailed in Table IV at the rated speed.

The repeatability of the spindown tests was evaluated by analyzing the standard deviation of measured losses across ten repetitions of each test. The standard deviations for the rated open circuit losses of the stator windings and mechanical losses were 1.7W and 1.2W, respectively. Averaged values were used in the efficiency calculations to ensure result accuracy against measurement noise. All the measured power loss curves are shown in Fig. 17.

The conducted tests, i.e., static torque measurement and spindown, are the optimal approaches to ensure that losses due to the electric machine specifics are separated from those caused by the drive system specifics. Hence, no voltage source inverter or control loop was involved throughout the testing, as the goal was to assess the effectiveness of the proposed loss mitigation techniques and the accuracy of FEA models without addressing power losses due to switching frequency harmonics and challenges with a control system, which are beyond the scope of this paper.

The measurements and FEA results collectively showcase a high level of consistency, encompassing torque and back-EMF constants, as well as phase resistance and inductance. The experimentally measured eddy current losses through spindown tests (Fig. 17) at the rated speed are less than 15% of the total rated losses, and the circulating current losses are below 1W, as reported in Table IV. The slight difference between the measured and calculated eddy current losses is due to the manufacturing tolerances in the PCB coils fabrication process. These results underscore the effectiveness of the proposed methods for loss reduction. The machine exhibits an efficiency of 95.8% under rated conditions, where it delivers 19Nm at 2100rpm, classifying the machine as ultra-

TABLE III
SPECIFICATIONS AND MAIN DIMENSIONS OF THE SELECTED OPTIMUM DESIGN FOR PROTOTYPING.

Parameter	Value	Unit
Rated power	4.18	kW
Rated speed	2,100	rpm
Torque density (natural cooling)	6.6	Nm/L
Airgap (magnet to stator)	1.3	mm
Stator thickness	6.0	mm
Rotor inner/outer diameter	208/304	mm
Stator inner/outer diameter	202/310	mm
No. of rotor/stator poles	36/36	-

TABLE IV
THE EXPERIMENTALLY MEASURED AND CALCULATED PARAMETERS AND POWER LOSSES OF THE PROTOTYPE MACHINE AT THE RATED CONDITION WHERE THE MACHINE IS DELIVERING 19NM AT 2100RPM.

Parameter	Exp.	Calc.	Unit
Torque constant	2.1	2.1	Nm/A
Phase resistance	0.57	0.55	Ω
Phase inductance	32.3	28.2	μH
Joule losses	129.5	125.4	W
Eddy current losses	22.6	24.7	W
Circulating current losses	≤ 1	0	W
Mechanical losses	30.4	30.4	W
Efficiency	95.8	95.8	%

premium efficiency (IE5 class) according to the IEC 60034-30-2 Standard.

VI. DISCUSSION

A. Phase Arrangements

The back-EMF waveforms depicted at the rated speed in Fig. 16 exhibit a 2.7% imbalance, with the phase A and C windings generating higher back-EMF as they are closer to the rotor magnets. In the case of the designed machine, the voltage imbalance level falls below the standard limit. The use of thicker PCB stators to accommodate more MMF leads to a higher voltage imbalance and torque ripple. A potential solution is to consolidate all three phases onto a single PCB stator. However, it poses significant challenges and complexities in implementation. An alternative method involves employing two identical sets of windings, meaning two PCB stators per phase, and arranging the phases as A-B-C-A-B-C along the axial direction. Note that separation of phases as shown in Fig. 3, provides useful phase insulation.

B. Skin and Proximity Effects

The skin effect refers to the inclination of high-frequency currents to travel along the outer surface of a conductor. The proximity effect involves the undesirable flow of current in alternate patterns, such as loops or concentrated distributions, caused by the magnetic fields produced by nearby conductors [34], [35]. The power losses in the windings due to skin and proximity effects were investigated in [34], [36].

The absence of the skin effect in narrow copper traces on the PCB stator was explained in [10], [15], as the skin depth at the rated frequency ($<$1kHz) is considerably higher than the diameter of the conductors. Hence, there is no increase in copper losses across the speed range due to AC resistance.

The proximity effect in PCB stator windings, where coils are closely stacked on top of each other, should be studied. To investigate the presence of the proximity effect between coils in different layers, the flux linkage of the coil in the middle layer was monitored through FEA at two different states. First, all other coils were excited with the rated current, and second, they were not excited. As there was no difference in the monitored flux linkage, it can be stated that the proximity effect in the stator winding of coreless AFPM machines is negligible. It was also demonstrated by the authors in [15].

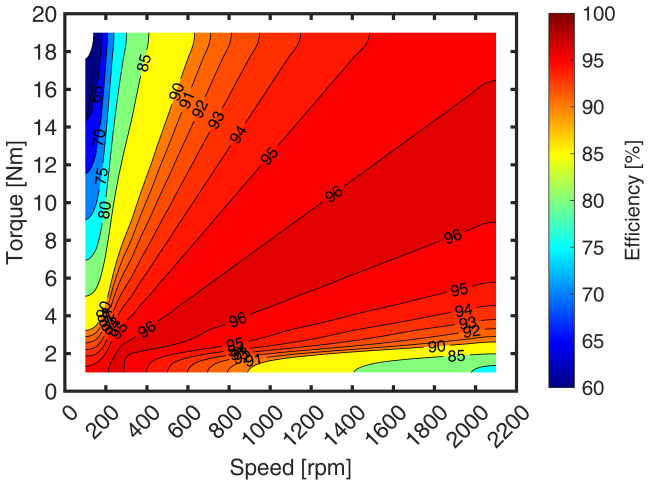

Fig. 18. The efficiency map of the prototype machine derived by scaling the experimentally measured torque and power losses.

To further investigate the proximity effect, the power losses of the prototype machine were measured in generator mode. The output power and losses of the generator were measured at 30% and 60% electric loading while keeping the shaft speed constant by controlling the prime mover. Using the phase current and stator resistance, the Joule loss was separated from the total losses. The results analysis showed that frequency-dependent power losses, including eddy and circulating current losses, remained constant. There were no additional losses as electrical loading increased, indicating that proximity losses are negligible.

C. Efficiency Map

Lack of stator core saturation effects in coreless machines results in a linear relationship between output torque and input current up to at least the rated value [24]. According to (8), eddy current losses are directly proportional to the square of the operating frequency, i.e., shaft speed. Mechanical losses, including bearing and windage losses, are proportional to the square of the shaft speed [32]. Therefore, utilizing the scaling logic outlined, the efficiency map of the machine can be derived by scaling the experimentally measured output torque and power losses (Table IV), as illustrated in Fig. 18.

This map reveals that the machine has a high efficiency over a wide speed range. Under heavy loading conditions and at high speeds, the machine exhibits higher efficiency due to the absence of frequency-dependent core losses and significantly reduced eddy and circulating current losses. For the prototype machine, an ultra-high efficiency of approximately 96% was experimentally verified at the rated torque of 19Nm and 2,100rpm.

D. Challenges with the Control Systems

Lack of a magnetic core and consequently very low phase inductance, as reported in Table IV, in coreless machines leads to some challenges in their control systems. Firstly, high current ripple and total harmonic distortion (THD) in inverter-fed coreless machines may result in additional power losses and performance degradation. Voltage source inverters based on wide bandgap semiconductor devices with high switching frequency can be employed to address this issue.

Low phase inductance also limits the flux weakening capability of the machine, narrowing down the constant power mode region. Better utilization of the inverter DC link or the addition of a boost converter stage to the drive system can potentially improve the machine's constant power operation. These challenges and the effectiveness of the aforementioned solutions were presented by the same group of authors in [37].

E. PCB Coils and Conventional Litz Wires

The PCB stator technology has the potential of lower cost, especially for high volume production, as compared with the more traditional Litz wire constructions, which require not only special and expensive electric wire, but also special coils on a supporting stator structure. Furthermore, it is expected that the manufacturing of PCB stators, which is highly repeatable, require less capital investment for highly automated production.

In principle, a major limitation with the PCB technology is represented by the potentially relatively high eddy current losses. The present paper addresses this challenge and proposes novel methods of equivalent transposition of the PCB traces, series and parallel connection of the equivalent coils, which result in very low eddy current losses, comparable with those from the more expensive Litz wire typical designs.

VII. Conclusion

This paper presented a systematic design procedure for PCB stator coreless AFPM machines, taking into account the minimization of all stator loss components, as well as PCB manufacturing limitations and standards. The efficacy of the proposed design procedure was showcased by designing a coreless PCB stator AFPM machine for fan applications.

The designed machine was prototyped, and the effectiveness of the proposed loss mitigation techniques, and the accuracy of the 3D FEA models were experimentally validated. This validation included spindown tests, as well as measurements of static torque and back-EMFs. The experimental results demonstrated a high level of agreement with the analytical calculations and 3D FEA simulations.

Eddy current losses were significantly reduced without adversely affecting Joule losses. This was achieved by designing PCB coils with a narrow width and relatively thick copper traces in the axial direction, considering multiple parallel paths. Circulating current losses within parallel paths were virtually eliminated with the implementation of the proposed layer transposition technique, which balances the flux linkages within the coils in different layers. The experimentally measured power losses indicated a 96% efficiency at the rated condition, delivering 4.2kW at 2,100rpm.

Acknowledgment

This paper is based upon work supported by the National Science Foundation (NSF) under Award No. #1809876. Any opinions, findings, and conclusions, or recommendations expressed in this material are those of the authors and do not necessarily reflect the views of the NSF. The support of Regal Rexnord Corp., Ansys Inc., and University of Kentucky, the L. Stanley Pigman Chair in Power Endowment is also gratefully acknowledged.

References

[1] M. Rosu, P. Zhou, D. Lin, D. Ionel, M. Popescu, F. Blaabjerg, V. Rallabandi, and D. Staton, *"Multiphysics Simulation by Design for Electrical Machines, Power Electronics and Drives"*, J. Wiley - IEEE Press, 2017.

[2] F. Nishanth, J. Van Verdeghem, and E. L. Severson, "A review of axial flux permanent magnet machine technology," *IEEE Transactions on Industry Applications*, vol. 59, no. 4, pp. 3920–3933, 2023.

[3] F. Marcolini, G. De Donato, F. G. Capponi, M. Incurvati, and F. Caricchi, "Novel multiphysics design methodology for coreless axial flux permanent magnet machines," *IEEE Transactions on Industry Applications*, pp. 1–11, 2023.

[4] V. Rallabandi, N. Taran, D. M. Ionel, and J. F. Eastham, "Coreless multidisc axial flux PM machine with carbon nanotube windings," *IEEE Transactions on Magnetics*, vol. 53, no. 6, pp. 1–4, 2017.

[5] MachineDesign, "Axial flux motor topology signals next generation of electric motors," 2024. [Online]. Available: https://www.machinedesign.com/mechanical-motion-systems/article/21281110/axial-flux-motor-topology-signals-next-generation-of-electric-motors

[6] P. Guedes-Pinto and R. A. Lee, "System, method and apparatus for direct liquid-cooled axial flux electric machine with PCB stator," U.S. Patent US11 482 908B1, 2021.

[7] R. Wang and A. Kamper, "Evaluation of eddy current losses in axial flux permanent magnet (AFPM) machine with an ironless stator," in *Conference Record of the 2002 IEEE Industry Applications Conference. 37th IAS Annual Meeting*, vol. 2, 2002, pp. 1289–1294.

[8] G. François and B. Dehez, "Impact of slit configuration on eddy current and supply current losses in PCB winding of slotless PM machines," *IEEE Transactions on Industry Applications*, vol. 58, no. 5, pp. 6035–6044, 2022.

[9] F. Copt, C. Koechli, and Y. Perriard, "Minimizing the circulating currents of a slotless BLDC motor through winding reconfiguration," in *2015 IEEE Energy Conversion Congress and Exposition (ECCE)*, 2015, pp. 6497–6502.

[10] Y. Chulaee, D. Lewis, A. Mohammadi, G. Heins, D. Patterson, and D. M. Ionel, "Circulating and eddy current losses in coreless axial flux PM machine stators with PCB windings," *IEEE Transactions on Industry Applications*, vol. 59, no. 4, pp. 4010–4020, 2023.

[11] O. Taqavi and S. Mirimani, "Design aspects, winding arrangements and applications of printed circuit board motors: A comprehensive review," *IET Electric Power Applications*, vol. 14, pp. 1505–1518, 09 2020.

[12] F. Tokgöz, G. Çakal, and O. Keysan, "Comparison of PCB winding topologies for axial-flux permanent magnet synchronous machines," *IET Electric Power Applications*, 2020.

[13] X. Wang, W. Pang, P. Gao, and X. Zhao, "Electromagnetic design and analysis of axial flux permanent magnet generator with unequal-width PCB winding," *IEEE Access*, vol. 7, pp. 164 696–164 707, 2019.

[14] F. Marcolini, G. De Donato, F. G. Capponi, and F. Caricchi, "Design of a high speed printed circuit board coreless axial flux permanent magnet machine," in *2021 IEEE Energy Conversion Congress and Exposition (ECCE)*, 2021, pp. 4353–4360.

[15] N. Salim, S. P. Nikam, S. Pal, A. K. Wankhede, and B. G. Fernandes, "Multiphysics analysis of printed circuit board winding for high-speed axial flux permanent magnet motor," *IET Electric Power Applications*, vol. 13, no. 6, pp. 805–811, 2019.

[16] B. Anvari, P. Guedes-Pinto, and R. Lee, "Dual rotor axial flux permanent magnet motor using PCB stator," in *2021 IEEE International Electric Machines Drives Conference (IEMDC)*, 2021, pp. 1–7.

[17] F. Tokgoz, Gülsuna, F. Karakaya, G. Cakal, and O. Keysan, "Mechanical and thermal design of an optimized PCB motor for an integrated motor drive system with GaNFETs," *IEEE Transactions on Energy Conversion*, vol. 38, no. 1, pp. 653–661, 2023.

[18] M. G. Kesgin, P. Han, N. Taran, D. Lawhorn, D. Lewis, and D. M. Ionel, "Design optimization of coreless axial-flux PM machines with litz wire and PCB stator windings," in *2020 IEEE Energy Conversion Congress and Exposition (ECCE)*, 2020, pp. 22–26.

[19] P. Han, D. Lawhorn, Y. Chulaee, D. Lewis, G. Heins, and D. M. Ionel, "Design optimization and experimental study of coreless axial-flux PM machines with wave winding PCB stators," in *2021 IEEE Energy Conversion Congress and Exposition (ECCE)*, 2021, pp. 4347–4352.

[20] D. Lawhorn, P. Han, D. Lewis, Y. Chulaee, and D. M. Ionel, "On the design of coreless permanent magnet machines for electric aircraft propulsion," in *2021 IEEE Transportation Electrification Conference Expo (ITEC)*, 2021, pp. 278–283.

[21] A. Hembel and B. Sarlioglu, "PCB winding for electric machines with integrated 3D printed heat exchanger," in *2022 IEEE Transportation Electrification Conference Expo (ITEC)*, 2022, pp. 421–426.

[22] Y. Chulaee, G. Heins, B. Robinson, M. Thiele, D. Patterson, and D. M. Ionel, "Design optimization considering a detailed pcb stator layout for coreless afpm machines with minimal eddy and circulating current losses," in *2023 IEEE Energy Conversion Congress and Exposition (ECCE)*, 2023, pp. 3753–3758.

[23] *Ansys Electronics Desktop, Maxwell, version 23.1, 2023, ANSYS Inc.*

[24] Y. Chulaee, D. Lewis, M. Vatani, J. F. Eashtam, and D. M. Ionel, "Torque and power capabilities of coreless axial flux machines with surface PMs and halbach array rotors," in *2023 IEEE International Electric Machines and Drives Conference (IEMDC)*, 2023, pp. 1–6.

[25] D. Ionel, J. Eastham, T. Miller, and E. Demeter, "Design considerations for permanent magnet synchronous motors for flux weakening applications," *IEE Proceedings-Electric Power Applications*, vol. 145, no. 5, pp. 435–440, 1998.

[26] Y. Chulaee and D. M. Ionel, "Ultra-fast finite element analysis of coreless axial flux permanent magnet synchronous machines," *IET Electric Power Applications*. [Online]. Available: https://ietresearch.onlinelibrary.wiley.com/doi/abs/10.1049/elp2.12439

[27] N. Taran, V. Rallabandi, G. Heins, and D. M. Ionel, "Systematically exploring the effects of pole count on the performance and cost limits of ultrahigh efficiency fractional HP axial flux PM machines," *IEEE Transactions on Industry Applications*, vol. 56, no. 1, pp. 117–127, 2020.

[28] N. Taran, D. M. Ionel, V. Rallabandi, G. Heins, and D. Patterson, "An overview of methods and a new three-dimensional FEA and analytical hybrid technique for calculating AC winding losses in PM machines," *IEEE Transactions on Industry Applications*, vol. 57, no. 1, pp. 352–362, 2021.

[29] P. Zhang, G. Y. Sizov, J. He, D. M. Ionel, and N. A. O. Demerdash, "Calculation of magnet losses in concentrated-winding permanent-magnet synchronous machines using a computationally efficient finite-element method," *IEEE Transactions on Industry Applications*, vol. 49, no. 6, pp. 2524–2532, 2013.

[30] F. Marcolini, G. De Donato, F. G. Capponi, and F. Caricchi, "Design of a high speed printed circuit board coreless axial flux permanent magnet machine," in *2021 IEEE Energy Conversion Congress and Exposition (ECCE)*, 2021, pp. 4353–4360.

[31] V. Rallabandi, N. Taran, D. M. Ionel, and P. Zhou, "Inductance testing for ipm synchronous machines according to the new ieee std 1812 and typical laboratory practices," *IEEE Transactions on Industry Applications*, vol. 55, no. 3, pp. 2649–2659, 2019.

[32] G. Heins, D. M. Ionel, D. Patterson, S. Stretz, and M. Thiele, "Combined experimental and numerical method for loss separation in permanent-magnet brushless machines," *IEEE Transactions on Industry Applications*, vol. 52, no. 2, pp. 1405–1412, 2016.

[33] A. S. Nagorny, R. H. Jansen, and D. M. Kankam, "Experimental performance evaluation of a high speed permanent magnet synchronous motor and drive for a flywheel application at different frequencies," *17th International Conference on Electrical Machines (ICEM 2006)*, pp. 1–6, 2006.

[34] C. Sullivan, "Optimal choice for number of strands in a litz-wire transformer winding," *IEEE Transactions on Power Electronics*, vol. 14, no. 2, pp. 283–291, 1999.

[35] A. Fatemi, D. M. Ionel, N. A. O. Demerdash, D. A. Staton, R. Wrobel, and Y. C. Chong, "Computationally efficient strand eddy current loss calculation in electric machines," *IEEE Transactions on Industry Applications*, vol. 55, no. 4, pp. 3479–3489, 2019.

[36] M. Popescu and D. G. Dorrell, "Skin effect and proximity losses in high speed brushless permanent magnet motors," in *2013 IEEE Energy Conversion Congress and Exposition*, 2013, pp. 3520–3527.

[37] Y. Chulaee, A. Mohammadi, A. Cramer, and D. M. Ionel, "Flexible control for wide speed range operation of high polarity stator coreless afpm machines with wbg semiconductor devices," in *2023 IEEE Energy Conversion Congress and Exposition (ECCE)*, 2023, pp. 4783–4788.